Simulations of the L–H transition dynamics with different heat and particle sources*

Li Hui-Dong(李会东)[a], Wang Zhan-Hui(王占辉)[b]†, Jan Weiland[c], Feng Hao(冯 灏)[a]‡, and Sun Wei-Guo(孙卫国)[a,d]

[a] School of Science, Research Center for Advanced Computation, Xihua University, Chengdu 610039, China
[b] Southwestern Institute of Physics, Chengdu 610041, China
[c] Department Applied Physics, Chalmers. University of Technology and Euratom-VR Association, S41296 Gothenburg, Sweden
[d] Institute of Atomic and Molecular Physics, Sichuan University, Chengdu 610065, China

(Received 2 April 2015; revised manuscript received 22 July 2015; published online 9 October 2015)

It is crucial to increase the total stored energy by realizing the transition from a low confinement (L-mode) state to a high confinement (H-mode) state in magnetic confinement fusion. The L–H transition process is simulated by using the predictive transport code based on Weiland's fluid model. Based on the equilibrium parameters obtained from equilibrium fitting (EFIT) in the experiment, the electron density n_e, electron temperature T_e, ion temperatures T_i, ion poloidal V_p, and toroidal momenta V_t are simulated self-consistently. The L–H transition dynamic behaviors with the formation of the transport barriers of ion and electron temperatures, the electron density, and the ion toroidal momenta are analyzed. During the L–H transition, the strong poloidal flow shear in the edge transport barrier region is observed. The crashes of the electron and ion temperature pedestals are also observed during the L–H transition. The effects of the heating and particle sources on the L–H transition process are studied systematically, and the critical power threshold of the L–H transition is also found.

Keywords: magnetic fusion, tokamak plasma, L–H transition, transport barriers

PACS: 52.35.Py, 52.70.La, 52.55.Tn, 52.55.Fa **DOI:** 10.1088/1674-1056/24/11/115204

1. Introduction

It is crucial to increase the total stored energy by realizing the transition from a low confinement (L-mode) state to a high confinement (H-mode) state in magnetic confinement fusion. The H-mode is usually characterized by an edge pedestal, in which the plasma will achieve a longer global energy confinement time and a higher plasma pressure.[1] It is critical for ignition and burning plasma operation, which is viewed as a key operation mode for future burning plasma experiments and the ultimate fusion reactors. The magnetic confinement plasma will make a spontaneous transition from a low confinement (L-mode) state to a high confinement (H-mode) state when the input heating power is strong enough and exceeds the critical heating power threshold.[2] The underlying physics behind the L–H transition has not been explained well to date. The H-mode operation can be controlled successfully and easily only when the physics of the L–H transition is really understood. Extensive research efforts have been made to control the L–H transition.[3] The L–H transition is characterized by a rapid suppression of the edge turbulence, a reduction of the D_α light emission intensity, the formation of a sharp edge pressure pedestal and a radial electronic well, an increase of the $\boldsymbol{E}\times\boldsymbol{B}$ shearing rate, and the formation of particle and energy transport barriers.[4] The L–H transition has been studied experimentally and theoretically.[4–8] The importance of the $\boldsymbol{E}\times\boldsymbol{B}$ flow shear for the L–H transition has been recognized.[5] One of the most convincing explanations for the L–H transition is the suppression of turbulence by the $\boldsymbol{E}\times\boldsymbol{B}$ flow shearing effects,[5] which have been proved by many experiments in the tokamaks.

Most of the experiments have reached the conclusion that the realization of the L–H transition requires sufficient plasma heating and fueling sources to exceed the power threshold, meanwhile it can trigger the formation of an edge transport barrier.[6] The underlying physics and especially the dynamics near the power threshold of the L–H transition have not been revealed, although some theoretical models have been proposed[3,6,7,9–12] and the theoretical studies of the L–H transition have been reviewed in Ref. [13]. Thus, the research on the L–H transition is still the present hottest topic of tokamak plasma. To obtain a long pulse H-mode discharge, there are still lots of experiments and simulations focusing on the key factors of the L–H transition and the evolution principles of the relevant physical quantities.[10,14–29] Among the theoretical models proposed for the L–H transition, the fluid model proposed by Weiland[30] is one of the well-known models to

*Project supported by the Funds of the Youth Innovation Team of Science and Technology in Sichuan Province, China (Grant No. 2014TD0023), the National Natural Science Foundation of China (Grant Nos. 11447228 and 11205053), and the China National Magnetic Confinement Fusion Science Program (Grant No. 2013GB107001).

†Corresponding author. E-mail: zhwang@swip.ac.cn
‡Corresponding author. E-mail: fenghao@mail.xhu.edu.cn

© 2015 Chinese Physical Society and IOP Publishing Ltd

reveal the L–H transition process, which has been utilized to simulate and realize the L–H transition in EAST tokamak.[31] The Weiland model is the main part of the MMM,[32] it has been benchmarked and validated in many studies,[33–35] and it has also been used by some theoretical researchers,[36,37] to study the particle transport.

In the present work, the model is used for simulating the L–H transition dynamics in tokamak plasma. The theoretical model is described in Section 2. The simulation results are presented in Section 3. Finally, the principal results are summarized in Section 4.

2. Theoretical model

The Weiland's fluid model[30,31] is used in the simulations. This model is capable of presenting the turbulent transport flux, the self-consistent radial force balance equation provides an $\boldsymbol{E}\times\boldsymbol{B}$ flow shear depending on the mean profiles, and finally the $\boldsymbol{E}\times\boldsymbol{B}$ flow shear gives feedback to the transport.

The edge boundaries of the density and the temperature are fixed at the values taken from the experiment. Sometimes they will be modified within the experimental error bars. The inner boundaries are flat. For the poloidal rotation, the boundary condition is taken as the initial edge neoclassical $v_{\rm nc}$. For the toroidal rotation, the boundary condition is set to be $-100\,v_{\rm nct}$, where $v_{\rm nct}$ is the projection of the neoclassical rotation in the toroidal direction.

In the model, the transport dynamic information is mainly contained in the particle flux $\Gamma_{{\rm P}\alpha}$, the momentum flux $\Phi_{{\rm i}\alpha}$, and the energy flux Q_α. They are usually parameterized by analogy to Fick's law as follows:

$$\Gamma_{{\rm P}\alpha} = -D_\alpha \frac{\partial n_\alpha}{\partial r}, \tag{1}$$

$$\Phi_{{\rm i}\alpha} = -\chi_{{\rm i}\alpha} \frac{\partial u_{{\rm i}\alpha}}{\partial r}, \tag{2}$$

$$Q_\alpha = -\chi_\alpha \frac{\partial T_\alpha}{\partial r}. \tag{3}$$

The foundational equations of the Weiland model are the reactive reduced Braginskii multi-fluid equations. The fluid resonance effect is also included in the energy equation as shown below

$$\frac{3}{2} n_{\rm j} \left(\frac{\partial}{\partial t} + \boldsymbol{v}_{\rm j} \cdot \boldsymbol{\nabla} \right) T_{\rm j} + p_{\rm j} \boldsymbol{\nabla} \cdot \boldsymbol{v}_{\rm j} = -\nabla \cdot \boldsymbol{q}_{\rm j}, \tag{4}$$

where

$$\boldsymbol{q}_{\rm j} = \boldsymbol{q}_{*{\rm j}} = \frac{5}{2} \frac{P}{m_{\rm j} \Omega_{\rm cj}} (\boldsymbol{e}_{//} \times \nabla T_{\rm j}), \tag{5}$$

$$\frac{\delta T_{\rm j}}{T_{\rm j}} = \frac{\omega}{\omega - 5\omega_{\rm Dj}/3} \left[\frac{2}{3} \frac{\delta n_{\rm j}}{n_{\rm j}} + \frac{\omega_{*{\rm e}}}{\omega} \left(\eta_{\rm j} - \frac{2}{3} \right) \frac{e\phi}{T_{\rm e}} \right]. \tag{6}$$

Here, the convective diamagnetic part of $\nabla \cdot \boldsymbol{q}$ cancels other convective diamagnetic parts in the energy equation, thus there is only the curvature part left which gives rise to the perpendicular fluid resonance.

The saturation level of the electric potential without flow shear is

$$\frac{e\phi}{T_{\rm e}} = \frac{\gamma}{k_\theta c_{\rm s} k_{\rm r} \rho_{\rm s}} = \frac{\gamma}{\omega_*} \frac{1}{k_{\rm r} L_{\rm n}}. \tag{7}$$

By using the Waltz rule[38,39] and replacing the flow shear rate with

$$\gamma \to \gamma - \omega_{E\times B}, \tag{8}$$

we have

$$\frac{e\phi}{T_{\rm e}} = \frac{\gamma - \omega_{E\times B}}{k_\theta c_{\rm s} k_{\rm r} \rho_{\rm s}} = \frac{\gamma - \omega_{E\times B}}{\omega_*} \frac{1}{k_{\rm r} L_{\rm n}}, \tag{9}$$

where $k_{\rm r} \approx 1/L_{\rm r}$ and $L_{\rm r}$ is the radial correlation length. Then the transport will change from the simplest electrostatic ITG mode into the following form:[30]

$$\chi_{\rm i} = \frac{1}{\eta_{\rm i}} \left(\eta_{\rm i} - \frac{2}{3} - \frac{10}{9\tau} \varepsilon_{\rm n} \right) \times \frac{(\gamma - \omega_{E\times B})^3 / k_{\rm r}^2}{(\omega_{\rm r} - 5\omega_{\rm Di}/3)^2 + (\gamma - \omega_{E\times B})^2}. \tag{10}$$

From Eq. (10), we can see how the total saturation level influences the thermal diffusivity due to the combined influence of the $\boldsymbol{E}\times\boldsymbol{B}$ convection and the Waltz rule. The Waltz rule is always used for the transport, when the $\gamma - \omega_{E\times B} < 0$ holds, the mode will be turned off.

The flow shear rate can be written as

$$\omega_{E\times B} = \frac{r}{q} \frac{\partial}{\partial r} (q V_{E\theta}/r). \tag{11}$$

In order to calculate the flow shear rate as $V_{E\theta} = E_r/B$, we need to know the radial electric field obtained from the radial force balance

$$E_r = B_\theta V_\varphi - B_\varphi V_\theta + \frac{1}{e Z_{\rm i} n_{\rm i}} \frac{\partial P_{\rm i}}{\partial r}. \tag{12}$$

The toroidal flow will be simulated by the parallel momentum transport equation

$$m_{\rm i} n_{\rm i} \left(\frac{\partial}{\partial t} + 2\boldsymbol{U}_{\rm Di} \cdot \boldsymbol{\nabla} \right) \delta u_{||} = -m_{\rm i} n_{\rm i} \boldsymbol{u}_E \cdot \boldsymbol{\nabla} U_{||0} - \left[\widehat{e}_{||} \cdot \boldsymbol{\nabla} + U_{||0} \frac{m_{\rm i} \boldsymbol{U}_{D_{\rm i}}}{T_{\rm i}} \cdot \boldsymbol{\nabla} \right] \times \left(\delta p_{\rm i} + e n_{\rm i} \phi - \frac{\omega + \omega_{*{\rm e}}(1+\eta_{\rm e})/\tau}{k_{||} c} A_{||} \right), \tag{13}$$

or

$$\delta u_{||} = -\frac{k_\theta D_B}{\omega - 2\omega_{\rm Di}} \frac{{\rm d}U_{||0}}{{\rm d}r} + \frac{\langle k_{||} \rangle + \omega_{\rm Di} U_{||0} / (\tau \cdot c_{\rm s}^2)}{\omega - 2\omega_{\rm Di}} \times \left(\delta p + n e \phi - \frac{\omega + \omega_{*{\rm e}}(1+\eta_{\rm e})/\tau}{k_{||} c} A_{||} \right) / (m_{\rm i} n_{\rm i}), \tag{14}$$

where

$$U_{\rm Di} = 2\frac{T_{\rm i}}{eB^2}\widehat{n}\times\nabla B, \tag{15}$$

$$D_B = \frac{T_{\rm e}}{eB}. \tag{16}$$

The toroidal rotation averaging over time and spatial scales of the fluctuations is calculated as follows:

$$\Gamma_{||} = \langle v_{\rm Er}\delta u_{||}\rangle \approx \Gamma_\phi. \tag{17}$$

The toroidal momentum transport is calculated in the usual way as

$$\frac{\partial U_\phi}{\partial t} + \frac{\partial}{\partial r}\Gamma_\phi = S_v. \tag{18}$$

The poloidal flux is given by the Reynolds stress as

$$\Gamma_{\rm p} = \langle V_{\rm Er}V_\theta\rangle = -D_B^2 k_{\rm r}k_\theta\frac{1}{2}\widehat{\phi}^*\left[\widehat{\phi}+\frac{1}{\tau}\widehat{p}_i\right] + {\rm c.c.} \tag{19}$$

Then

$$\frac{\partial U_\theta}{\partial t} + \frac{\partial}{\partial r}\Gamma_{\rm p} = S_v, \tag{20}$$

where

$$S_v = 0.67\nu_{\rm ii}(v_\theta - v_{\rm nc})/\varepsilon,$$

$$\varepsilon = r/R. \tag{21}$$

Here the neoclassical rotation $v_{\rm nc}$ is used.[40]

In the Weiland's fluid model, many different instabilities, such as the slab and toroidal ITG, trapped electron modes driven by charge separation, compression, or collisions, resistive ballooning modes,[30,41] MHD and kinetic ballooning modes, and peeling modes, are included. The relation between the drift type and the MHD type modes is explained by the parallel electric field which is obtained from the relation between the electrostatic and magnetic potentials. The MHD type modes, particularly the kinetic ballooning modes and peeling modes, are important in the H-mode plasma. The MHD type modes and drift type modes are included all the time. The physics conditions will determine which modes are the most important, while they will coexist.

To obtain this, the following free electron continuity and parallel momentum equations are used:

$$\frac{\partial n_{\rm ef}}{\partial t} + \nabla\cdot\left[n_{\rm ef}\left(v_E + v_{*e} + v_{\|0}\frac{\delta B_\perp}{B} + v_{\|}\widehat{e}_{\|}\right)\right] = 0, \tag{22}$$

$$\frac{\partial n_{\rm ef}}{\partial t} = \frac{e}{T_{\rm e}}\left(\phi + \frac{\omega_{*\rm e}-\omega}{k_{\|}}A_{\|}\right) + {\rm i}\frac{v_{\|\rm e}}{k_{\|}D_{\rm e}}. \tag{23}$$

Combining the above two equations, we can obtain

$$\frac{eA_{\|}}{T_{\rm e}} = k_{\|}\frac{\omega-\omega_{*\rm e}}{\omega(\omega-\omega_{*\rm e}) + \omega_{\rm De}(\omega_{*\rm eT}-\omega) - \dfrac{k_{\|}k_\theta T_{\rm e}\partial J_{\|0}}{e^2Bn_0\partial r} - k_\perp^2\rho_{\rm s}^2k_{\|}^2v_{\rm A}^2(1-{\rm i}\delta)}\frac{e\phi}{T_{\rm e}}, \tag{24}$$

where

$$\delta = \frac{\omega-\omega_{\rm De}}{k_{\|}^2D_{\rm e}}, \quad D_{\rm e} = \frac{T_{\rm e}}{m_{\rm e}\nu_{\rm e}}.$$

Quasi-neutrality will force the ion particle transport to be equal to electron particle transport (impurities are taken as a fixed fraction of the electron density). More details of this equation were given in Refs. [30] and [31].

3. Simulation results

3.1. Process of the L–H transition

The machine parameters used in the present simulation are as follows: the aspect ratio $\varepsilon = 0.24$, the elongation $\kappa = 1.05$, the minor radius $r_0 = 0.4$ m, and the major radius $R_0 = 1.65$ m. The equilibrium magnetic field $B_0 = 1.34$ T. The time step 10^{-5} s is used in the simulation. For obtaining a better resolution of the edge transport barriers, the normalized radial resolution domain is selected to be in a range from 0.63 to 1.0. The total input heating power $P_{\rm i}$ is about 0.6 MW. The deposition profile of the heating power and the profile of the edge particle source are shown in Fig. 1.

In order to study the L–H transition in detail, it is simulated for a long enough time to cover the whole period of the L–H transition, ~600 ms, with the heating power $P = 1.0P_{\rm i}$ and the edge source strength SEN = 1.0×10^{19} m$^3\cdot$s^{-1}. The plasma profiles at different times are plotted in Fig. 2. It can be seen that the height of the density barrier increases gradually with time going by. The heights of both electron and ion temperature barriers increase before $t = 200$ ms, but a sudden drop appears at $t = 250$ ms. The barrier heights of both the electron temperature and the ion temperature will go up again later, but they will not reach values as high as those at $t = 200$ ms. This process is clearly shown by the variations of ion and electron temperatures on the top of the pedestals (Fig. 2(d)). It seems that the barrier will crash and oscillate as time goes by, especially for the temperature profiles. The crash appears to be edge localized modes (ELMs), i.e., the gradient increases with time going by until it passes the MHD limits. Then the transport increases strongly and the gradients decrease back to the L-mode. The plasma is below the critical gradient and it will go back to the H-mode again with continuous heat and particle source.

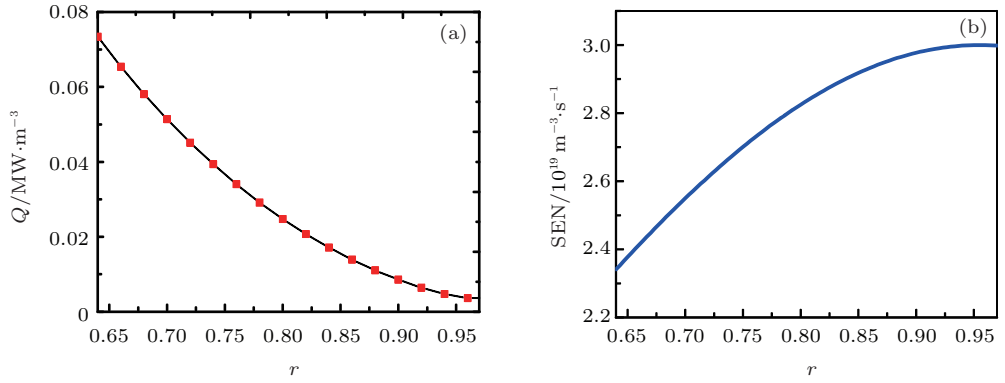


Fig. 1. (color online) (a) Deposition profile of the heating power and (b) profile of the edge particle source used in the simulation.

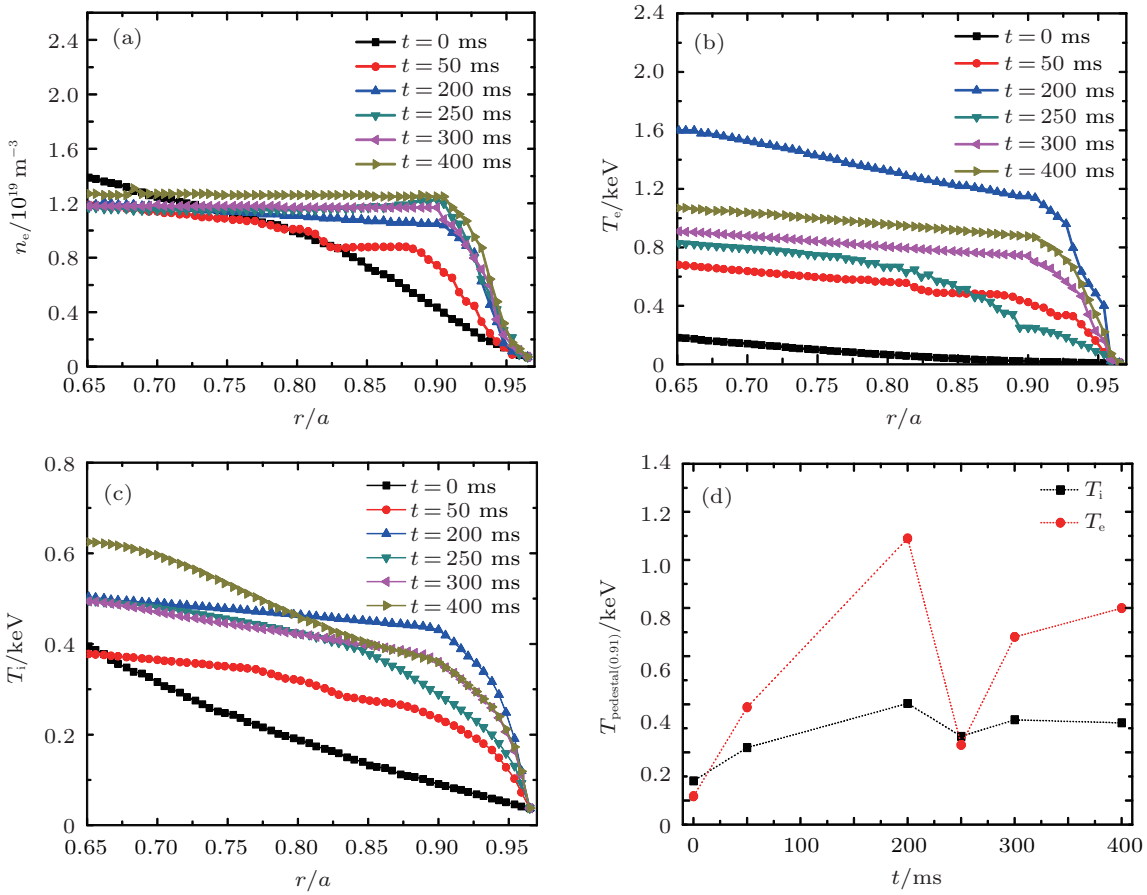


Fig. 2. (color online) Time evolutions of (a) electron density n_e, (b) electron temperature T_e, (c) ion temperature T_i profiles with the initial heating power P_i and the edge source SEN = 1.0×10^{19} m^{-3}·s^{-1}. (d) Variations of ion and electron temperatures on the top of the pedestals. The L–H transition process is observed, and the transport barriers are formed during the simulation.

Figure 2 shows the time evolutions of the mean plasma profiles. It is obvious that the L–H transitions occur and the pedestal heights increase gradually with continuously heating and fueling. To study the physics characters of the L–H transition in more detail, the simulation profiles at $t = 140$ ms are given in Fig. 3. The curves with squares are the initial profiles for each quantity, and the curves with circles are those simulated by Weiland's fluid model. The simulated profiles of electron density n_e, electron temperature T_e, ion temperature T_i, poloidal momentum V_p, and flow shear rate $\omega_{E\times B}$ all suggest that the edge transport barriers are formed, which indicates that the plasma is in the H-mode at the moment. The profiles of poloidal momentum V_p and flow shear $\omega_{E\times B}$ display strong edge shears, which reduce the turbulence intensity and play a key role in the L–H transition in tokamak plasma.[2,4,5] The toroidal momentum V_t profile forms a pedestal far from the edge of the plasma. The toroidal rotation is important for triggering the barrier since it can reduce or enhance the radial electric field due to the poloidal rotation. In the simulations, the initial profile of the poloidal rotation is entirely neoclassical while the toroidal rotation has a boundary (fixed) due to the intrinsic rotation.

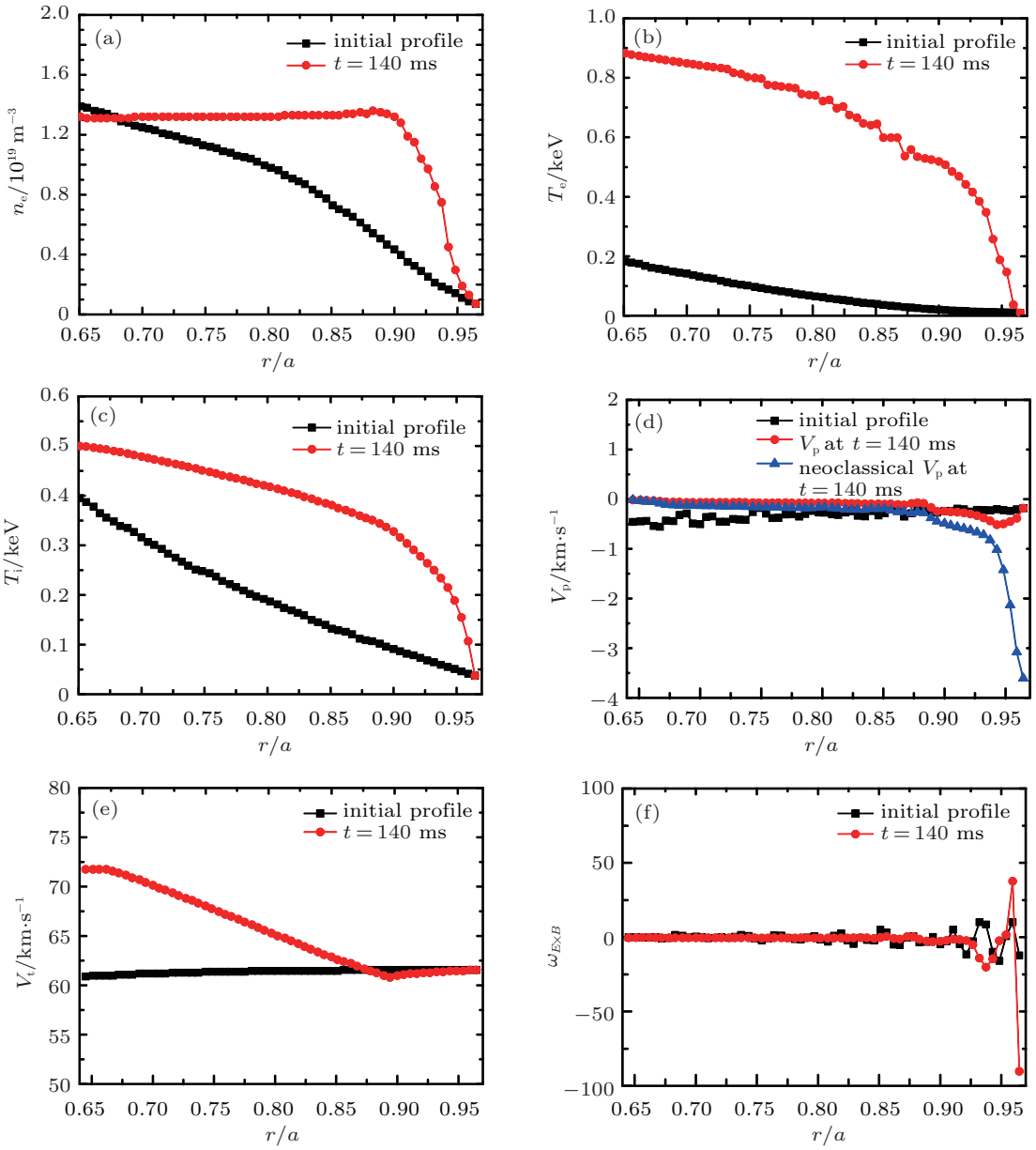


Fig. 3. (color online) Profiles of (a) electron density n_e, (b) electron temperature T_e, (c) ion temperature T_i, (d) poloidal velocity V_p, (e) toroidal velocity V_t (for velocity V, positive refers to the clockwise direction and negative the anticlockwise direction), and (f) the $\boldsymbol{E} \times \boldsymbol{B}$ flow shear rate $\omega_{E\times B}$ profiles (lines with circles) at $t = 140$ ms and the initial profiles at $t = 0$ ms (lines with squares). Transport barriers of the electron density, electron temperature, and the ion temperature produced. The flow shear near the boundary is observed.

3.2. Effects of heat and particle sources on the L–H transition

In order to study the effects of the heat and particle sources on the L–H transition, the profiles of electron density, electron temperature, and ion temperature varying at different time are simulated in the absence of the heat and particle sources. The initial ion temperature is higher than the electron temperature. The ion temperature decreases as time increases, while the electron temperature increases in the early time due to the energy interchange between electrons and ions. When the ions and the electrons are thermally balanced, the temperatures of both species will reduce simultaneously due to the radiation effect. The energy will transfer much faster from the hotter ions to the electrons in the core plasma due to collisions, thus the inner temperature decreases rapidly and the inner electron temperature increases much faster than the edge electron temperature, forming a pedestal-like structure. In the absence of the particle source, the density profile is almost stable (Fig. 4).

3.2.1. The effect of heat source on the L–H transition

In order to display the process of the barrier formation in more detail, the profiles of electron density, electron temperature, and ion temperature at different times are given with the increased heating power $1.5P_i$ in Fig. 5. Similar results to those predicted at a heating power of $1.0P_i$ are obtained. The density pedestal is set up gradually. It is about 50 ms from the initial simulation, the pedestals of electron density n_e and

temperature T_e become obvious, and the heights of the barriers increase slowly with time. Interestingly, the height of the electron temperature does not increase monotonically. It reaches a maximum at about $t = 80$ ms, comes down at about $t = 120$ ms, then goes back to a relatively large value at about $t = 140$ ms. It means for the crash of the electron barrier, however, no similar phenomena for the profiles of electron density and ion temperature are observed.

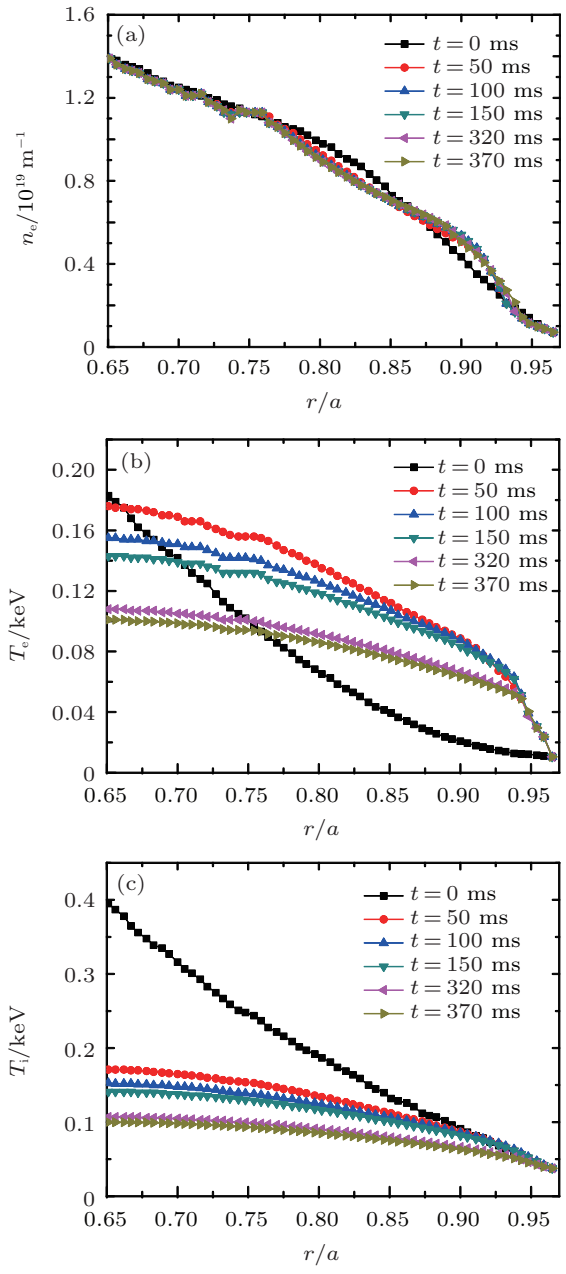


Fig. 4. (color online) Profiles of (a) density n_e, (b) electron temperature T_e, and (c) ion temperature T_i simulated in the absence of heat and particle sources.

The profiles of electron density n_e, electron temperature T_e, and ion temperature T_i at $t = 140$ ms with different heating powers are displayed in Fig. 6. As shown in the figure, the edge transport barriers of both density and temperature are not formed once the heating power is $0.1P_i$. With the increase of the heating power, the transport barriers are formed and become more and more apparent. The results indicate that the density barriers are formed more easily than the temperature barriers. The profiles also indicate that the density barrier and the ion temperature barrier will saturate when the heating power increases up to $1.5P_i$, while the electron temperature barrier still increases. The power threshold is about $0.5P_i$, ~ 0.3 MW, in our simulations. When the heating power is $0.5P_i$, the flow shear rate is even stronger than that simulated using the much higher heating powers $1.0P_i$, and $1.5P_i$. The underlying physics behind the L–H transition near the power threshold and the dependence of the power threshold on tokamak plasma conditions are complicated, which will be revealed in the further studies later.

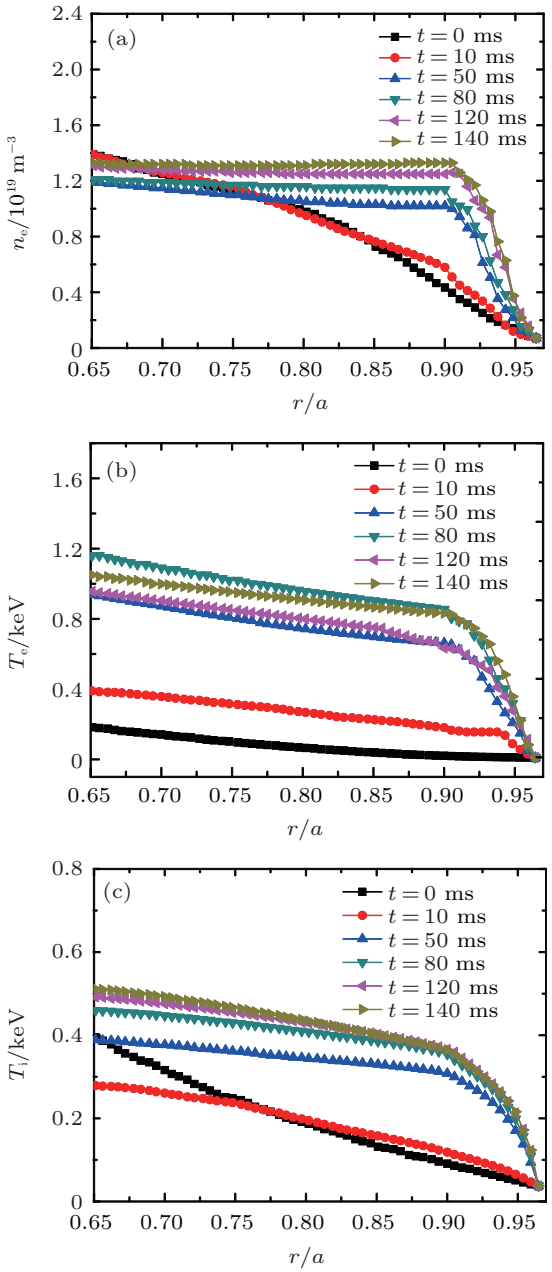


Fig. 5. (color online) Simulated profiles of (a) electron density n_e, (b) electron temperature T_e, and (c) ion temperature T_i at different time with the heat power $P = 1.5P_i$ and the edge source SEN = 3.0×10^{19} m^{-3}·s^{-1}.

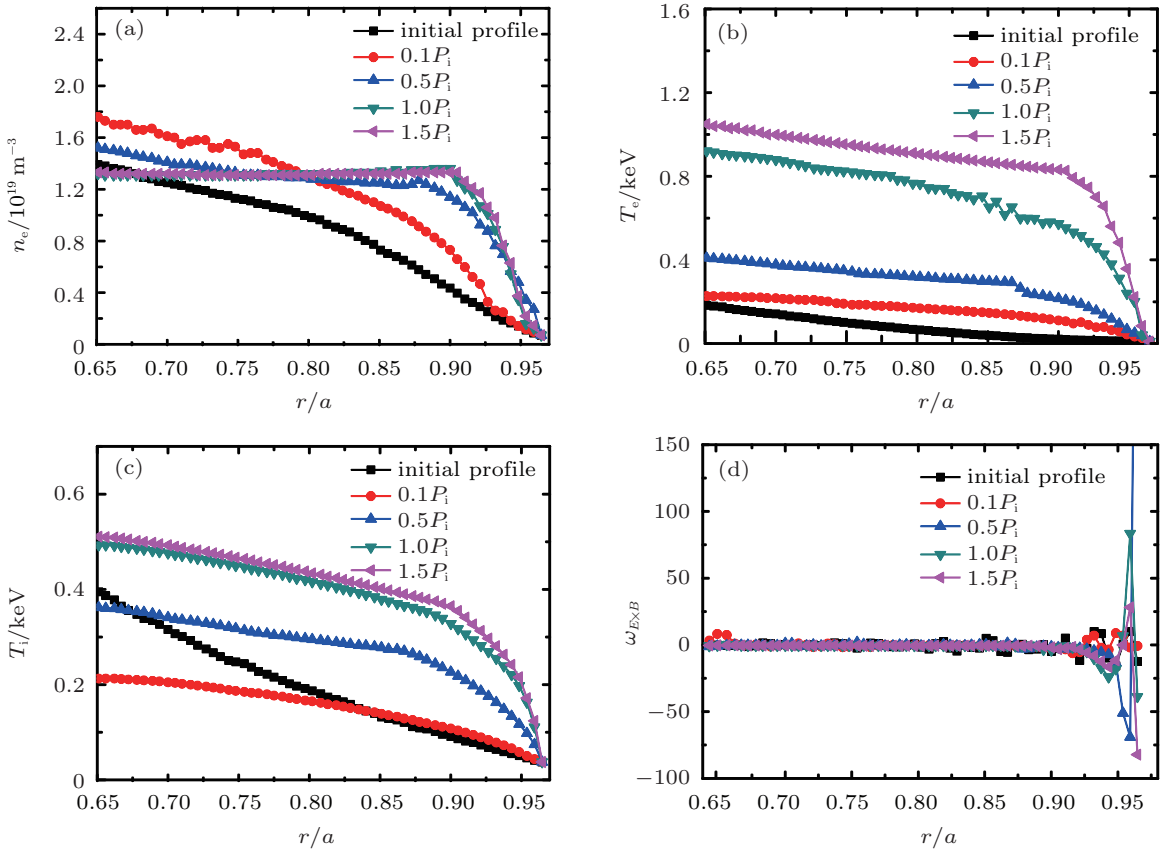


Fig. 6. (color online) Profiles of (a) simulated electron density n_e, (b) electron temperature T_e, (c) ion temperature T_i, and (d) flow shear rate $\omega_{E\times B}$ at $t = 140$ ms with different heat powers and fixed edge source SEN = 3.0×10^{19} m^{-3}·s^{-1}.

3.2.2. Effects of particle source on the L–H transition

In simulations of the transport barrier formation, a source is located near the plasma edge boundary. To study the influence of the edge source on the simulated profiles, several different sources are compared for two different heat power sources, $1.0P_i$ and $0.1P_i$, respectively (Figs. 7 and 8). Comparing the two sets ($1.0P_i$ and $0.1P_i$) of the simulated profiles, we can see that only enough heating power is necessary to form the transport barriers, which implies the existence of the power threshold. At low heating power, it is difficult to form a transport barrier even though there is a large enough particle source near the edge. The flow shear rate with low heating power is also much lower (Fig. 8) than that simulated with strong heating power (Fig. 7). When the heating power is strong enough, the height of the density barrier rises with the increase of the strength of the particle source. However, the temperature barrier will be restricted by the relatively strong edge particle source as the height of the temperature barrier decreases with the increase of the particle source as shown in Fig. 7. In this case, the flow shear rate $\omega_{E\times B}$ exhibits a similar trend to that of the temperature barrier, namely, a strong edge particle source will restrict the flow shear rate. Physically, when there is a strong particle source, the heating power will be diluted by more particles, then the temperatures will be reduced. It is natural that a strong particle source will produce a higher density transport barrier and lower temperature transport barriers.

4. Summary and discussion

The H-mode has been realized and the transport barriers are formed in the present L–H transition simulations based on the Weiland's fluid model. The effects of the heat and the particle sources on the L–H transition have been studied in the present paper. The results show that a strong enough heating power above the threshold is necessary to realize an L–H transition. With strong heating power, the height of the density pedestal increases nearly monotonically with the strength of the edge particle source increasing, however, the temperature pedestals do not perform similarly to that of the density pedestal, and it will be constrained by the stronger particle source. At low heating power, even though the particle source is strong enough, it is difficult to form the edge transport barrier.

The principal results in the present study are summarized as follows.

(i) The transition from the L mode to the H mode is realized by using the Weiland's fluid model. Apparent transport barriers for the density, electron temperature, ion temperature, and toroidal velocity are simulated and formed near the edge of the tokamak plasma.

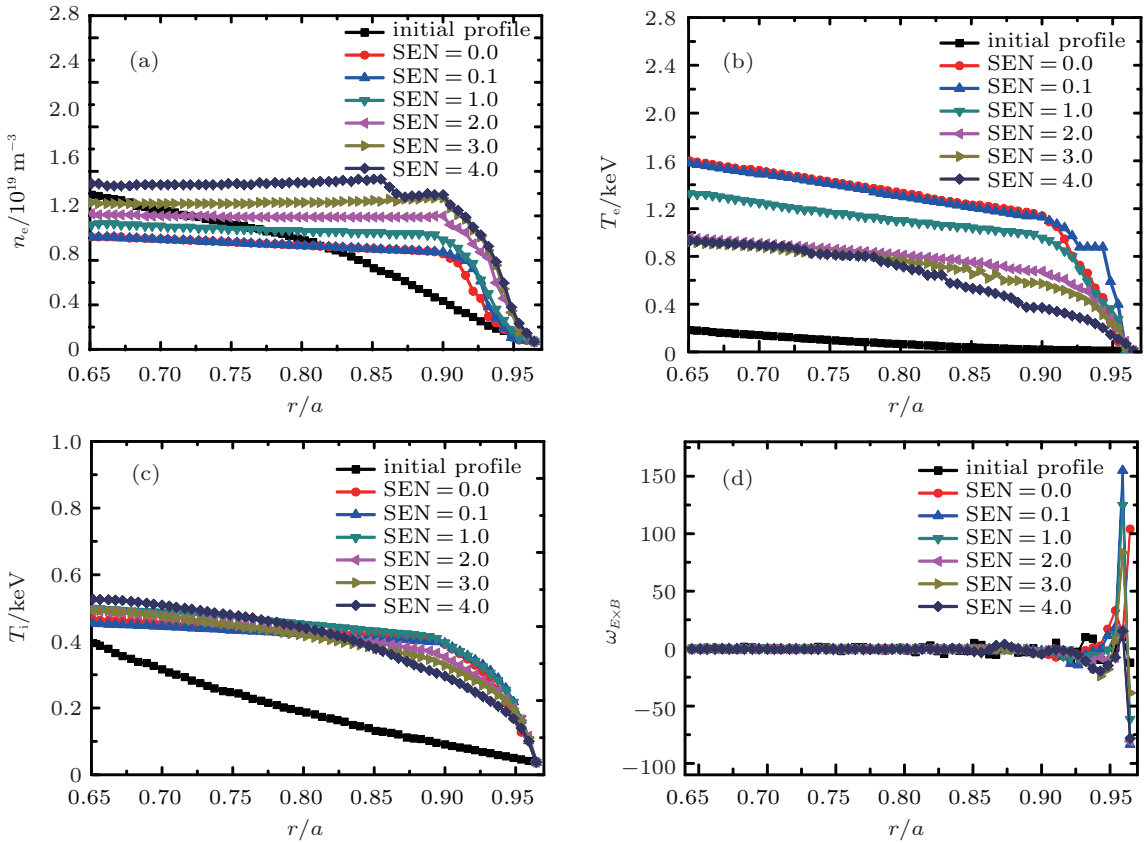


Fig. 7. (color online) Profiles of (a) density n_e, (b) electron temperature T_e, (c) ion temperature T_e, and (d) flow shear rate $\omega_{E\times B}$ at $t = 140$ ms with different edge particle sources when the heating power $P = 1.0P_i$.

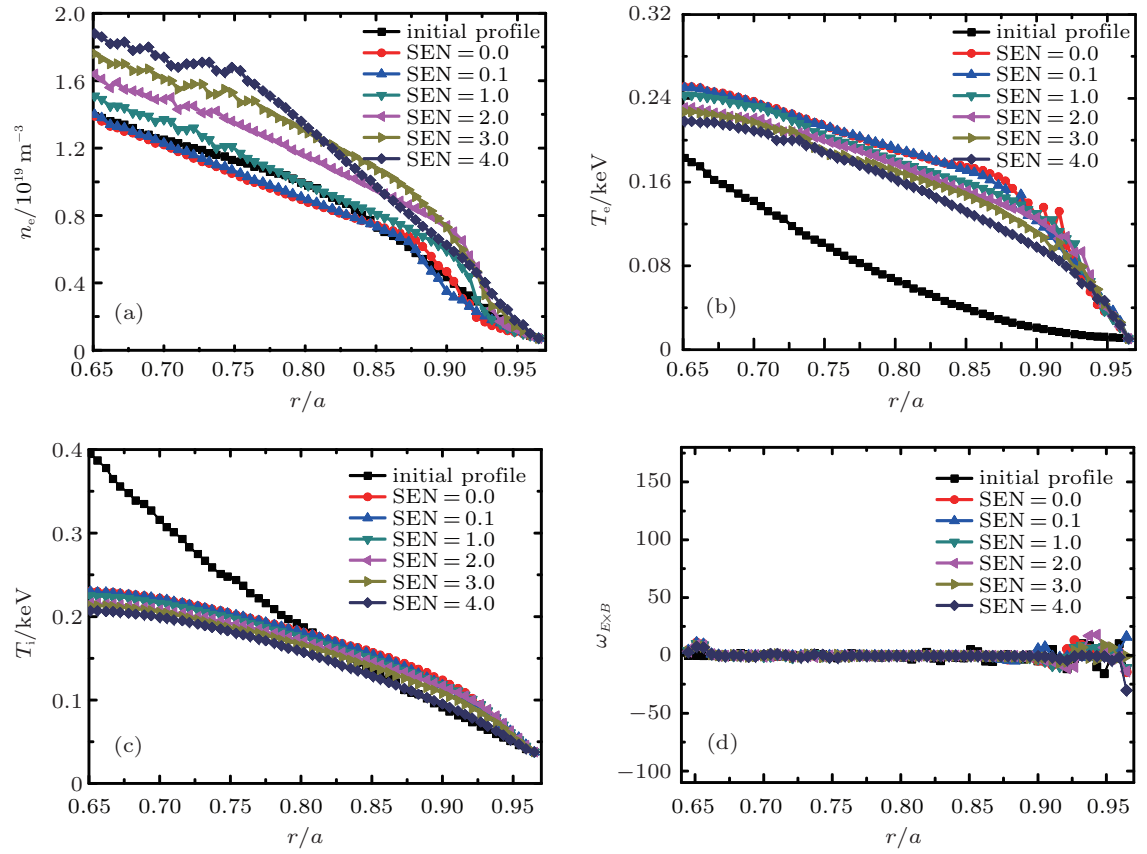


Fig. 8. (color online) Profiles of (a) density n_e, (b) electron temperature T_e, (c) ion temperature T_e, and (d) flow shear rate $\omega_{E\times B}$ at time $t = 140$ ms with different edge particle sources when the heating power $P = 0.1P_i$.

(ii) The power threshold is found to be in a range of about $0.5P_i$, ~ 0.3 MW, for the occurrence of the L–H transition through the present simulation, and this power threshold will be influenced by the strength of the edge particle source. At a strong heating power, the height of the density barrier rises with the increase of the strength of the particle source. The temperature barrier will be restricted by the strong edge particle source, and the height of the temperature barrier will decrease when the particle source increases.

(iii) The heights of the transport barriers of the electron temperature and the ion temperature seem to crash with the increase of time, especially for the electron temperature, and this kind of crash appears to be related to the occurrence of the ELMs.

(iv) The dynamic characteristics during the L–H transition are studied: the strong poloidal velocity and flow shear are predicted near the edge of the plasma.

In the following study, the evolution of MHD instabilities during the L–H transition will be investigated. Also, some transport characteristics of the tokamak plasma, such as the transport coefficients, the magnetic shear, and the flow shear, near the threshold power can be further studied. The underlying physics of the L–H transition near the power threshold and the dependence of the power threshold on the tokamak plasma conditions will be studied later. Some other physical process, including the I-phase process and the L–I–H or H–I–L transition, can also be studied in the coming research.

Acknowledgement

The authors wish to thank Wang A K, Wang G Q, Ma J, Xu M, Wang Z T, Zhong W L, and Xia F for their fruitful discussion.

References

[1] Wagner F, Fussmann G, Grave T, Keilhacker M, Kornherr M, Lackner K, McCormick K, Muller E R, Stabler A, Becker G, Bernhardi K, Ditte U, Eberhagen A, Gehre O, Gernhardt J, Gierke G V, Glock E, Gruber O, Haas G, Hesse M, Janeschitz G, Karger F, Kissel S, K1über O, Lisitano G, Mayer H M, Meisel D, Mertens V, Murrnann M, Poschenrieder W, Rapp H, Rohr H, Ryter F, Schneider F, Siller G, Smeulders P, Soldner F, Speth E, Steuer K H, Szymanski Z and Vollmer O 1984 *Phys. Rev. Lett.* **53** 1453

[2] Keilhacker M 1987 *Plasma Phys. Control. Fusion* **29** 1401

[3] Miki K, Diamond P H, Fedorczak N, Gürcan Ö D, Malkov M, Lee C, Kosuga Y, Tynan G, Xu G S, Estrada T, McDonald D, Schmitz L and Zhao K J 2013 *Nucl. Fusion* **53** 073044

[4] Yan Z, McKee G R, Fonck R, Gohil P, Groebner R J and Osborne T H 2014 *Phys. Rev. Lett.* **112** 125002

[5] Burrell K H 1997 *Phys. Plasmas* **4** 1499

[6] Miki K, Diamond P H, Hahn S H, Xiao W W, Gürcan Ö D and Tynan G R 2013 *Phys. Rev. Lett.* **110** 195002

[7] Kim E and Diamond P H 2003 *Phys. Rev. Lett.* **90** 185006

[8] Estrada T, Hidalgo C, Happel T and Diamond P H 2011 *Phys. Rev. Lett.* **107** 245004

[9] Fundamenski W, Militello F, Moulton D and McDonald D C 2012 *Nucl. Fusion* **52** 062003

[10] Xu G S, Shao L M, Liu S C, Wang H Q, Wan B N, Guo H Y, Diamond P H, Tynan G R, Xu M, Zweben S J, Naulin V, Nielsen A H, Rasmussen J J, Fedorczak N, Manz P, Miki K, Yan N, Chen R, Cao B, Chen L, Wang L, Zhang W and Gong X Z 2014 *Nucl. Fusion* **54** 013007

[11] Weymiens W, Blank H J and Hogeweij G M D 2013 *Phys. Plasmas* **20** 082306

[12] Dam M, Brøns M and Rasmussen J J 2013 *Phys. Plasmas* **20** 102302

[13] Connor J W and Wilson H R 2000 *Plasma Phys. Control. Fusion* **42** R1

[14] Leconte M, Diamond P H and Xu Y 2014 *Nucl. Fusion* **54** 013004

[15] Willensdorfer M, Fable E, Wolfrum E, Aho-Mantila L, Aumayr F, Fischer R, Reimold F, Ryter F and the ASDEX Upgrade Team 2013 *Nucl. Fusion* **53** 093020

[16] Bourdelle C, Maggi C F, Chôné L, Beyer P, Citrin J, Fedorczak N, Garbet X, Loarte A, Millitello F, Romanelli M, Sarazin Y and JET EFDA Contributors 2014 *Nucl. Fusion* **54** 022001

[17] Ryter F, Barrera Orte L, Kurzan B, McDermott R M, Tardini G, Viezzer E, Bernert M, Fischer R and The ASDEX Upgrade Team 2014 *Nucl. Fusion* **54** 083003

[18] Xu G S, Wang H Q and Xu M 2014 *Nucl. Fusion* **54** 103002

[19] Cziegler I, Tynan G R, Diamond P H, Hubbard A E, Hughes J W, Irby J and Terry J L 2014 *Plasma Phys. Control. Fusion* **56** 075013

[20] Estrada T, Ascasíbar E, Blanco E, Cappa A, Diamond P H, Happel T, Hidalgo C, Liniers M, Ph van Milligen B, Pastor I, Tafalla D and the TJ-II Team 2012 *Plasma Phys. Control Fusion* **54** 124024

[21] Miki K, Diamond P H, Hahn S H, Xiao W W, Gürcan Ö D and Tynan G R 2013 *Phys. Plasmas* **20** 082304

[22] Chôné L, Beyer P, Sarazin Y, Fuhr G, Bourdelle C and Benkadda S 2014 *Phys. Plasmas* **21** 070702

[23] Müller S H, Conway G D, Birkenmeier G, Carralero D, Happel T, Herrmann A, Manz P, de Marné P, Mlynek A, Müller H W, Potzel S, Rohde V, Stroth U, Tsalas M, Tynan G R, Wolfrum E and ASDEX Upgrade Team 2014 *Phys. Plasmas* **21** 042301

[24] Stacey W M, Sayer M H, Floyd J P and Groebner R J 2013 *Phys. Plasmas* **20** 012509

[25] Battaglia D J, Chang C S and Kaye S M 2013 *Nucl. Fusion* **53** 113032

[26] Tynan G R, Xu M, Diamond P H, Boedo J A, Cziegler I, Fedorczak N, Manz P, Miki K, Thakur S, Schmitz L, Zeng Z, Doyle E J, McKee G M, Yan Z, Xu G S, Wan B N, Wang H Q, Guo H Y, Dong J, Zhao K, Cheng J, Hong W Y and Yan L W 2013 *Nucl. Fusion* **53** 073053

[27] Wu G J, Zhang X D, Li Y D, Sun P J and Cao G M 2014 *Nucl. Fusion* **54** 083030

[28] Feng B B, Yao L H, Chen C Y, Ji X Q, Zhong W L, Shi Z B, Yu D L, Cui Z Y, Song X M and Duan X R 2013 *Acta Phys. Sin.* **62** 015203 (in Chinese)

[29] Du H L, Sang C F, Wang L, Sun J Z, Liu S C, Wang H Q, Zhang L, Guo H Y and Wang D Z 2013 *Acta Phys. Sin.* **62** 245206 (in Chinese)

[30] Weiland J 2012 *Stability and Transport in Magnetic Confinement Systems* (New York : Springer) p. 1

[31] Weiland J 2014 *Phys. Plasmas* **21** 122501

[32] Rafiq T, Kritz A H, Weiland J, Pankin A Y and Luo L 2013 *Phys. Plasmas* **20** 032506

[33] Ma J, Wang G, Weiland J, Rafiq T and Kritz A H 2015 *Phys. Plasmas* **22** 012304

[34] Garzotti L, Garbe X, Mantica P, Parail V, Valovič M, Corrigan G, Heading D, Jones T T C, Lang P, Nordman H, Pégourié B, Saibene G, Spence J, Strand P, Weiland J and contributors to the EFDA-JET Work programme 2003 *Nucl. Fusion* **43** 1829

[35] Weiland J, Crombe K, Mantica P, Naulin V, Tala T and the JETEFDA Contributors 2011 *AIP Conference Proceedings- American Institute of Physics* **1392** 85

[36] Garzotti L, Garbet X, Mantica P and Parail V 2003 *Nucl. Fusion* **43** 1829

[37] Garbet X, Garzotti L and Mantica P 2003 *Phys. Rev. Lett.* **91** 035001

[38] Waltz R E, Kerbel G O and Milovich J 1994 *Phys. Plasmas* **1** 2229

[39] Zagorodny A and Weiland J 2009 *Phys. Plasmas* **16** 052308

[40] Staebler G M, Waltz R E and Wiley J C 1997 *Nucl. Fusion* **37** 287

[41] Singh R and Weiland J 1999 *Phys. Plasmas* **6** 1397